nature communications

Article | Article in Press

https://doi.org/10.1038/s41467-026-79434-4

Dual-functional-unit modulation enables superior energy storage in high-entropy relaxor ferroelectrics

Received: 8 July 2026

Accepted: 17 October 2026

Published online: 18 November 2026

Check for updates

Guanfu Liu[1,4], Jiyu Wang[2,4], Bao Ou[1,4], Xiqi Chen[1], Xuanyu Chen[1], Yi Cheng[1], Ran Gao[1], Bin Li[1] ✉, He Qi[3] ✉ & Yejing Dai[1] ✉

High-performance dielectric capacitors are indispensable for next-generation pulsed power systems. However, simultaneously achieving high recoverable energy density and efficiency remains challenging because of the intrinsic trade-off between polarization and breakdown strength. Here, we develop a dual-functional-unit modulation strategy to overcome this limitation in $Bi_{0.47}Na_{0.47}Ba_{0.06}TiO_3$-based ceramics through configurational-entropy engineering combined with microstructural optimization. Specifically, configurational entropy simultaneously tailors two key local functional units, namely local polarization configurations and oxygen octahedral tilt configurations. Multicomponent substitution at the A site (Ba^{2+}) and B site (Zn^{2+}/Nb^{5+}) induces fragmented heterogeneous polarization configurations together with weakened and disordered oxygen octahedral tilt, enabling strong field-induced polarization, highly reversible polarization responses, and enhanced intrinsic breakdown strength. Combined with grain refinement and improved densification achieved by high-energy ball milling, which further enhances electrical homogeneity and suppresses interfacial polarization, the optimized ceramic exhibits a breakdown strength of 94 kV mm^{-1}, a large recoverable energy density of 16.19 J cm^{-3} and a high efficiency of 91.3%. This work establishes dual-functional-unit modulation as an effective design principle for high-entropy relaxor ferroelectrics and provides a general framework for overcoming the polarization-breakdown trade-off in dielectric energy storage materials.

Efficient dielectric capacitors are indispensable for next-generation pulsed power systems because of their ultrahigh power density, ultrafast charge–discharge capability, and outstanding operational stability[1–3]. Nevertheless, compared with other electrical energy storage technologies, such as batteries and electrochemical capacitors, dielectric ceramics still suffer from relatively low recoverable energy density (W_{rec}) and energy storage efficiency (η), which severely restrict their applications in miniaturized, integrated, and lightweight electronic systems[4–6]. Developing dielectric ceramics that simultaneously deliver high W_{rec} and η has therefore become a central challenge for advanced capacitive energy storage.

The energy storage performance of dielectric ceramics is fundamentally governed by their electric-field-induced polarization behavior. Specifically, W_{rec} and η are jointly determined by the dielectric

[1]School of Materials, Shenzhen Campus of Sun Yat-sen University, Shenzhen, China. [2]State Key Laboratory of Advanced Electromagnetic Technology, Huazhong University of Science and Technology, Wuhan, China. [3]School of Materials Science and Technology, Hainan University, Hainan, China. [4]These authors contributed equally: Guanfu Liu, Jiyu Wang, Bao Ou. ✉e-mail: libin75@mail.sysu.edu.cn; qihe@hainanu.edu.cn; daiyj8@mail.sysu.edu.cn

breakdown strength (E_b) and the polarization difference (ΔP=P_{max}−P_r), where P_{max} and P_r denote the maximum and remanent polarization, respectively[6,7]. According to the calculation principles shown in Supplementary Fig. S1, achieving superior energy storage performance requires the simultaneous realization of large P_{max}, small P_r, and high E_b. However, these parameters are intrinsically coupled. Strong ferroelectric ordering generally favors large polarization but simultaneously results in pronounced hysteresis and reduced breakdown strength, leading to the long-standing trade-off between polarization response and breakdown resistance. Overcoming this intrinsic trade-off is therefore the key prerequisite for developing high-performance dielectric energy storage materials.

Relaxor ferroelectrics (RFEs), characterized by nanoscale polar nanoregions (PNRs) and highly reversible polarization responses, have emerged as promising candidates for high-performance dielectric energy storage ceramics[8–12]. Recently, configurational-entropy engineering has attracted increasing attention as an effective strategy for constructing high-performance RFEs[13]. By introducing multiple cations with distinct ionic radii, valence states, and polarizabilities, local random fields, chemical disorder, and configurational entropy (S_{config}) are simultaneously enhanced, disrupting long-range ferroelectric ordering and promoting relaxor behavior. Particularly in high-entropy systems (S_{config}>1.5 R), the resulting heterogeneous local polarization configurations provide strong polarization fluctuations together with highly reversible polarization evolution, while the dispersed polarization landscape effectively homogenizes the internal electric-field distribution, contributing to enhanced intrinsic breakdown strength[14–16]. Despite these advantages, previous studies have predominantly focused on regulating polarization configurations, whereas other local structural factors governing polarization evolution have received far less attention.

Among these factors, oxygen octahedral (BO_6) tilt represents another fundamental local functional unit that strongly influences polarization behavior and structural stability[17–19]. Ordered BO_6 tilt is generally associated with delayed polarization saturation and enhanced structural anisotropy, which constrain polarization switching and increase hysteresis[20]. In contrast, lattice disorder induced by high configurational entropy can weaken, randomize, or even eliminate BO_6 tilt, thereby reducing structural constraints on polarization rotation and facilitating highly reversible polarization responses[21–23]. Therefore, local polarization configurations and BO_6 tilt configurations constitute two coupled local functional units that collectively determine polarization evolution under external electric fields. Nevertheless, their cooperative regulation has rarely been explored, and whether simultaneously tailoring these two local structural units can overcome the polarization–breakdown trade-off remains an open question.

Although configurational-entropy engineering effectively enhances the intrinsic breakdown strength, the ultimate dielectric breakdown behavior is also strongly influenced by extrinsic microstructural factors, including grain size, densification, defect concentration, and electrical homogeneity[24–26]. High-energy ball milling is an effective microstructural optimization approach capable of producing fine and homogeneous powders with enhanced sintering activity, thereby promoting grain refinement, improved densification, and suppressed abnormal grain growth[27–29]. The resulting dense and homogeneous microstructure effectively suppresses interfacial polarization and local electric-field concentration, providing additional enhancement of breakdown strength. Therefore, integrating local structural regulation with microstructural optimization offers a promising route for simultaneously maximizing intrinsic polarization performance and dielectric breakdown strength.

Here, we propose a dual-functional-unit modulation strategy to overcome the polarization-breakdown trade-off in $Bi_{0.47}Na_{0.47}Ba_{0.06}TiO_3$ (BNBT)-based RFEs through configurational-entropy engineering combined with high-energy ball milling (Fig. 1). Highly polarizable Zn^{2+} and Nb^{5+} ions are introduced into the B-site, primarily enhancing local random fields while maintaining large polarization response (Fig. 1a), whereas large-radius Ba^{2+} ions are incorporated into the A-site, predominantly contributing to lattice expansion and weakened BO_6 tilt (Fig. 1b)[30–32]. Consequently, a (1-x) $Bi_{0.47}Na_{0.47}Ba_{0.06}TiO_3$-$x$Ba($Zn_{1/3}Nb_{2/3}$)$O_3$ (100xBZN) system with a S_{config} increasing from 0.88 R to 1.80 R was established (Fig. 1c). The detailed calculation of S_{config} is provided in Supplementary Table S1. The high-entropy effect simultaneously tailors fragmented heterogeneous polarization configurations and weakened, disordered BO_6 tilt configurations (Fig. 1d), enabling strong field-induced polarization, highly reversible polarization responses, and enhanced intrinsic breakdown strength. Further combined with grain refinement and microstructural homogenization achieved by high-energy ball milling (Fig. 1e), the optimized ceramic achieves a high E_b of 94 kV mm^{-1}, together with a large ΔP (> 58 μC cm^{-2}), resulting in a large W_{rec} of 16.19 J cm^{-3} and a high η of 91.3% (Fig. 1f). This work establishes dual-functional-unit modulation as an effective design principle for high-entropy relaxor ferroelectrics and provides a general strategy for overcoming the polarization–breakdown trade-off in dielectric energy storage materials.

Results and discussion

Dielectric relaxation and domain evolution

X-ray diffraction patterns (Supplementary Fig. S2) confirm that all 100xBZN ceramics crystallize in a single-phase perovskite structure without detectable secondary phases. With increasing BZN content, the dielectric responses exhibit increasingly diffuse phase transitions and weakened temperature dependence (Supplementary Fig. S3), while Raman spectra show broadened vibrational modes in the 200–400 cm^{-1} range, indicating enhanced B-site chemical disorder (Supplementary Fig. S4). These results collectively demonstrate progressively enhanced dielectric relaxation with increasing S_{config}.

Piezoresponse force microscopy (PFM) results reveal a clear evolution of domain structures with increasing S_{config}, as shown in Fig. 2. The 0BZN sample exhibits well-defined ferroelectric stripe domains with characteristic sizes of several hundred nanometers, indicative of long-range ferroelectric ordering. Upon BZN incorporation, the domain contrast becomes progressively diffuse, suggesting the disruption of long-range ferroelectric ordering and the emergence of PNRs (Fig. 2a). The domain-switching behavior under an external electric field exhibits a strong dependence on S_{config}. To probe the dynamic domain response, a 10 × 10 μm^2 region was first poled at −30 V, followed by the application of progressively increasing positive voltages to four individual 2 × 2 μm^2 subregions (Fig. 2b). For 0BZN, clear domain switching is observed at 10 V, and the switched domains remain stable after relaxation, consistent with its relatively large P_{max} and P_r (Supplementary Fig. S5). In contrast, with increasing S_{config}, the phase contrast becomes gradually weaker and the switching threshold gradually increases, reaching ~40 V for 12BZN and 16BZN, ~60 V for 20BZN, and exceeding 60 V for 24BZN. More importantly, the fraction of switched regions that recover their initial states after relaxation increases with S_{config}, indicating that the PNRs exhibit progressively more dynamic and reversible responses to the external electric field (Fig. 2c). This observation is consistent with the enhanced relaxor behavior observed in the high-entropy compositions.

Energy storage performance

The polarization behavior under an external electric field is closely linked to S_{config}. As shown in Fig. 3a, the unipolar P–E loops of 100xBZN ceramics at a low electric field exhibit enhanced relaxor characteristics accompanied by reduced polarization hysteresis. According to the widely accepted criterion (S_{config} ≥ 1.5 R), once x ≥ 0.16, the system enters the high-entropy regime, where the

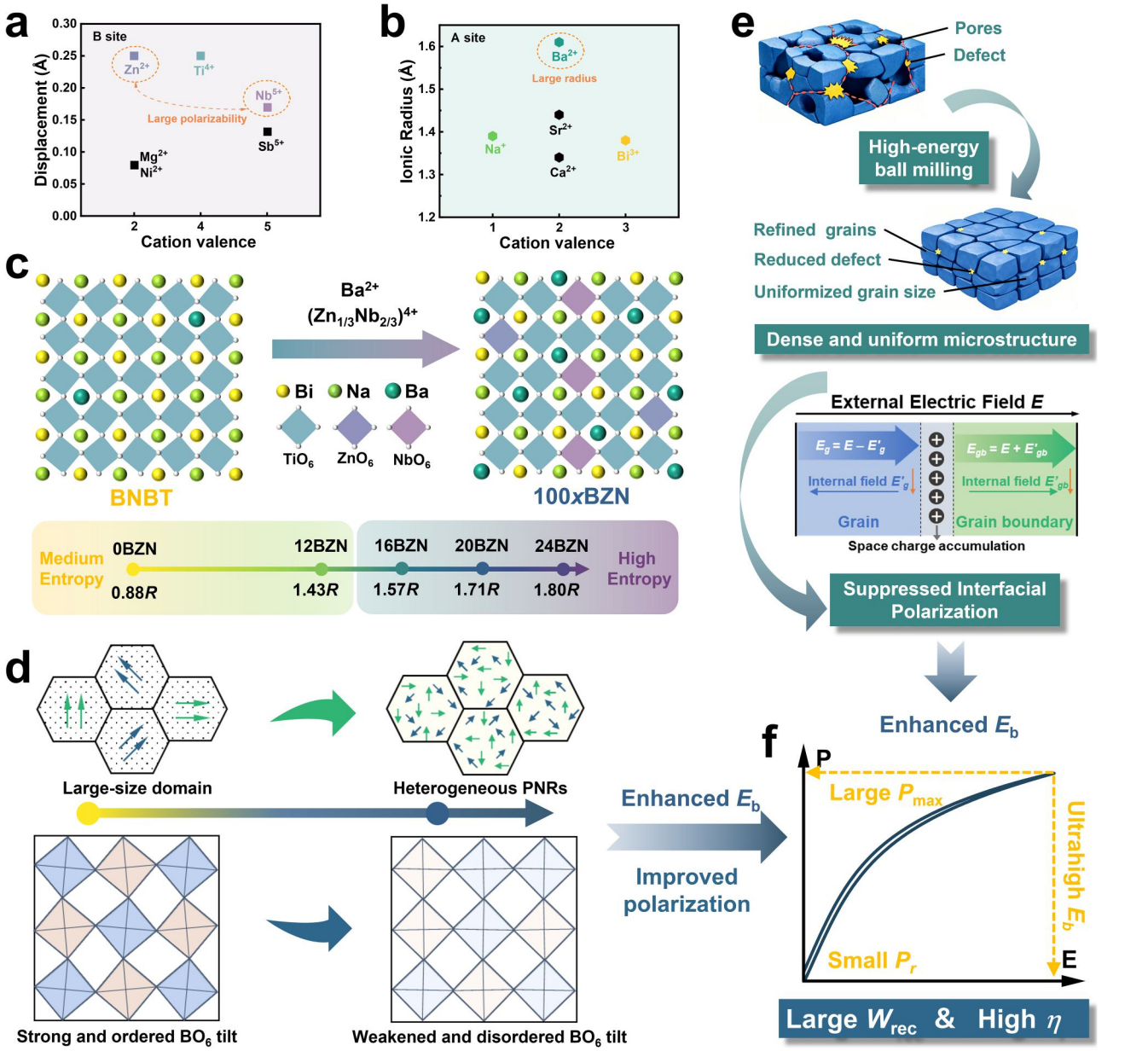


Fig. 1 | Schematic diagram of the dual-functional-unit modulation strategy. **a** Valence states and atomic displacements of B-site ions. **b** Valence states and ionic radii of A-site ions. **c** High-entropy engineering. **d** High-entropy-effect-driven evolution of the local structures. **e** Microstructural optimization and suppression of interfacial polarization via high-energy ball milling. **f** *P*–*E* loop improved by dual-functional-unit modulation.

hysteresis becomes nearly negligible, indicating highly reversible polarization responses. Under their respective breakdown electric fields, all high-entropy compositions display slim *P*–*E* loops characterized by large P_{max} (>50 μC cm^{-2}) and high E_b (>60 kV mm^{-1}), as shown in Fig. 3b. With increasing S_{config}, the E_b increases from 62 kV mm^{-1} (16BZN) to 77 and 80 kV mm^{-1} for 20BZN and 24BZN, respectively. The enhanced breakdown strength, together with the maintained high polarization, leads to a gradual increase in W_{rec}, reaching 10.28, 13.39, and 13.44 J cm^{-3} for 16BZN, 20BZN, and 24BZN, respectively (Fig. 3c and Supplementary Fig. S6). Meanwhile, the η remains consistently above 90%, demonstrating excellent stability under high electric fields. These results demonstrate that the high-entropy effect promotes highly reversible polarization and simultaneously enhances breakdown strength, providing an effective strategy for achieving ultrahigh energy storage density and efficiency in relaxor ferroelectric ceramics.

Further optimization of 20BZN through high-energy ball milling produces the 20BZN(H) ceramic with further enhanced energy storage performance. As shown in Fig. 3d, the E_b increases markedly from 77 to 94 kV mm^{-1}, accompanied by an increase in P_{max} from ~58 μC cm^{-2} to ~61 μC cm^{-2} while maintaining an extremely low P_r. Consequently, 20BZN(H) achieves a superior W_{rec} of 16.19 J cm^{-3} together with a high η of 91.3% (Fig. 3e and Supplementary Fig. S7). Compared with representative reported lead-free dielectric ceramics, 20BZN(H) exhibits a competitive combination of high W_{rec}, η and E_b (Supplementary Table S2). Such performance surpasses that of most reported lead-free dielectric ceramics, demonstrating its considerable competitive advantage (Fig. 3f). Furthermore, the E_b–P_{max} comparison shows that 20BZN(H) lies in the high-polarization/high-breakdown-strength region beyond the conventional performance limitation of lead-free dielectric ceramics (Supplementary Fig. S8), further evidencing the effective decoupling of the conventional trade-

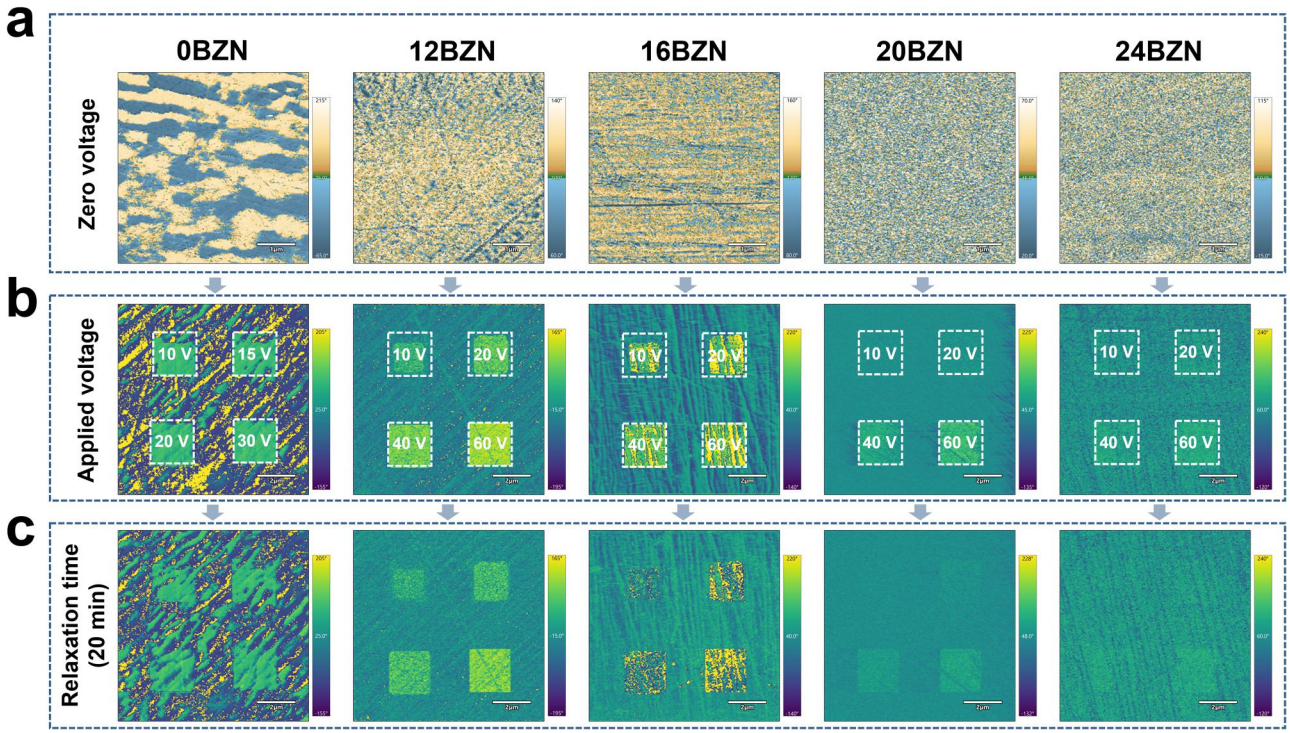


Fig. 2 | Out-of-plane PFM phase images of 100xBZN ceramics. a Before poling, **b** after poling under different applied voltages. **c** Evolution of the poled domains after relaxation for 20 min.

off between polarization and breakdown strength. In addition to its outstanding energy storage performance, 20BZN(H) exhibits excellent thermal and frequency stability (Supplementary Fig. S9). As shown in Fig. 3g, η remains above 90% over a wide temperature range of 20–120 °C, while W_{rec} shows only a slight variation of less than 3.4%. This stability is closely related to the temperature-insensitive phase structure (Supplementary Fig. S10). Similarly, both W_{rec} (<2.3%) and η (<5.6%) exhibit minimal fluctuations over the frequency range of 1–250 Hz (Fig. 3h), indicating excellent frequency robustness. Excellent fatigue resistance is also demonstrated, with both W_{rec} and η remaining nearly unchanged after 10^4 cycles (Supplementary Fig. S11). Furthermore, the ceramic delivers a high discharge energy density (W_D) of 8.68 J cm^{-3} with a fast discharge time ($t_{0.9} \approx 4.5$ μs) (Fig. 3i), demonstrating its capability for efficient energy release and its suitability for advanced pulsed-power energy storage applications. The lower W_D than W_{rec} reflects the difference between quasi-static and dynamic energy-storage processes. During rapid discharge, residual dielectric loss, charge-carrier conduction, and dynamic polarization relaxation inevitably dissipate part of the stored energy, while parasitic losses in the discharge circuit further reduce the practically delivered energy.

Local polarization configuration

Transmission electron microscopy (TEM) was employed to reveal the evolution of domain structures. As shown in Fig. 4a, 0BZN displays large ferroelectric domains within a nanodomain matrix, while 20BZN(H) lacks long-range ordered domain structures. HRTEM observations reveal PNRs in both ceramics, with their sizes reduced from several tens of nanometers in 0BZN to only a few nanometers in 20BZN(H). These observations indicate that the high-entropy effect weakens the coupling among polar clusters, leading to a smaller size of PNRs. Further evidence is provided by the selected-area electron diffraction (SAED) analysis (Fig. 4b). The SAED patterns of 0BZN exhibit ooe/2 and ooo/2 superlattice spots (where o and e denote odd and even indices) along the $[001]_c$ and $[110]_c$ zone axes, respectively. These reflections are associated with in-phase and antiphase BO_6 tilts corresponding to the P4bm and R3c phases commonly observed in BNT-based ceramics[3,33]. In contrast, the superlattice reflections disappear in 20BZN(H), indicating a large suppression of BO_6 tilt. The diminished octahedral distortion is consistent with the reduced size of PNRs and weakened local structural correlations induced by the high-entropy effect.

To elucidate the effect of S_{config} on local polarization at the atomic scale, atomic-resolution high-angle annular dark-field scanning transmission electron microscopy (HAADF-STEM) images acquired along the $[001]_c$ zone axis were analyzed for both 0BZN and 20BZN(H). As schematically illustrated in Supplementary Fig. S12a, the local polarization symmetry was determined from the off-center displacement directions of B-site cations within perovskite unit cells defined by four nearest-neighbor A-site cations[34]. Fig. 4c, d show the HAADF-STEM images and the corresponding distributions of unit cell areas for 0BZN and 20BZN(H), respectively (the calculation method is provided in Supplementary Fig. S12b). Compared with 0BZN, 20BZN(H) exhibits a larger average unit cell area ($Area_{ave}$), further confirming the lattice expansion induced by Ba^{2+} incorporation. Such lattice expansion is expected to facilitate field-induced ionic displacement and thereby enhance the polarization response.

The corresponding polarization vector maps are presented in Fig. 4e, f, where the arrow color denotes the polarization direction, and the arrow length represents the polarization magnitude. Both samples exhibit heterogeneous polarization configurations characterized by short-range ordered polar regions embedded within an overall disordered matrix, in which rhombohedral (R) and tetragonal (T) polar regions coexist with nonpolar cubic (C) phases. However, notable differences are observed in their local polarization structures. In 0BZN, the polar regions are relatively large and spatially continuous, whereas in 20BZN(H) they are further fragmented into nanoscale regions (~1–3 nm) and exhibit a more diffuse distribution. Meanwhile, the fraction of the nonpolar C phase increases in 20BZN(H), where it is finely dispersed among the R and T polar

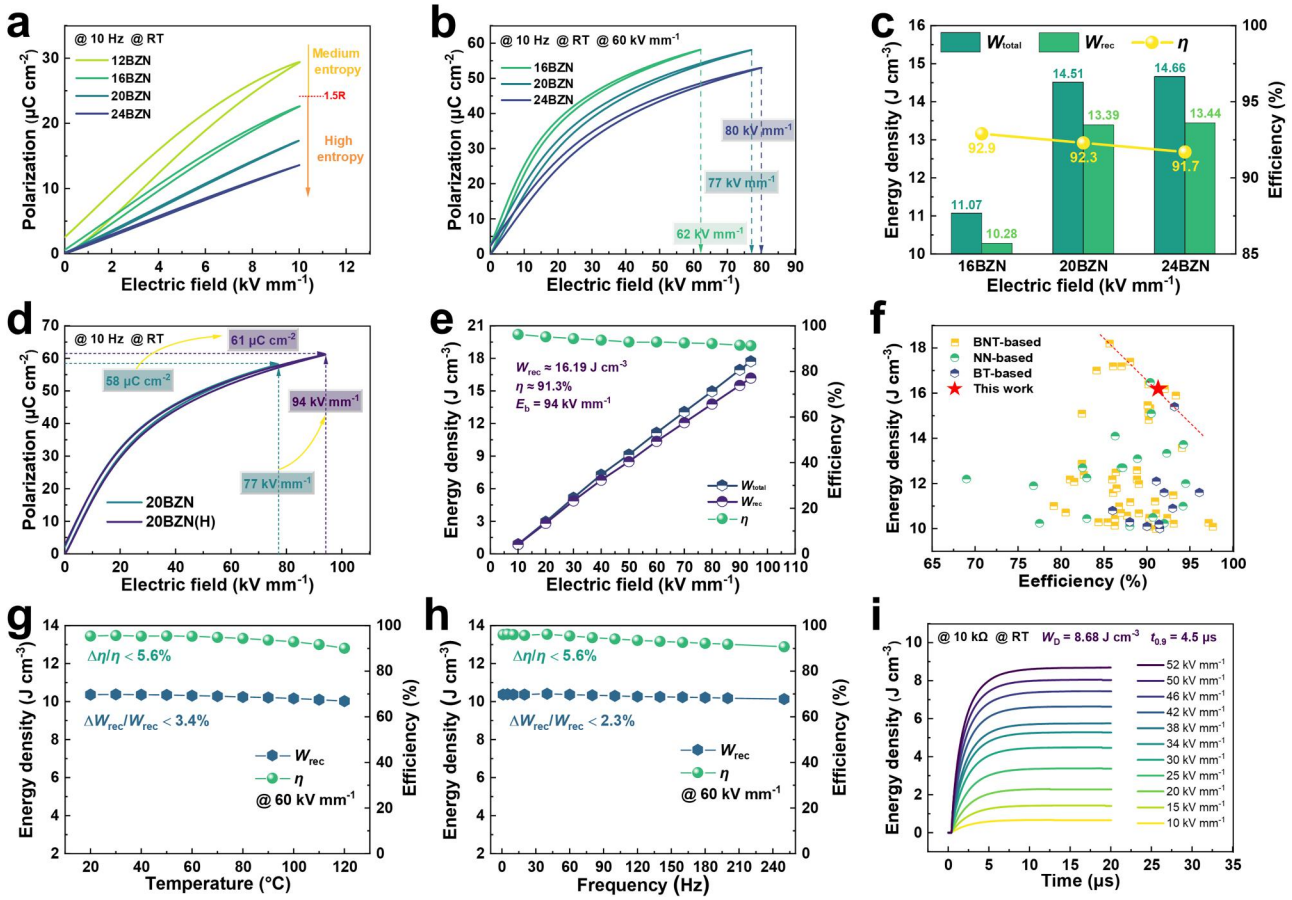


Fig. 3 | Energy storage performance of high-entropy 100*x*BZN ceramics. **a** Unipolar *P*–*E* loops of 12BZN, 16BZN, 20BZN, and 24BZN measured at 10 kV mm^{-1}. **b** Unipolar *P*–*E* loops of 16BZN, 20BZN, and 24BZN measured at their respective E_b, and **c** the corresponding W_{rec} and η values. **d** Unipolar *P*–*E* loops of 20BZN and 20BZN(H) measured at their respective E_b. **e** Energy storage density and efficiency of 20BZN(H) measured at various electric fields. **f** Comparison of W_{rec} and η between 20BZN(H) and other reported high-performance dielectric ceramics (data in Supplementary Table S2). **g** Temperature-dependent and **h** frequency-dependent W_{rec} and η of 20BZN(H) measured at 60 kV mm^{-1}. **i** W_D and $t_{0.9}$ obtained from overdamped discharge measurements under varying electric fields.

regions. The increased population of randomly distributed nonpolar regions is expected to reduce structural anisotropy and polarization anisotropy, thereby facilitating polarization rotation under an external electric field. Consistent with this structural evolution, the electric-field-dependent dielectric responses reveal a pronounced irreversible response in 0BZN, as evidenced by the distinct increasing- and decreasing-field curves, whereas 20BZN(H) exhibits nearly overlapping responses, indicative of highly reversible dielectric behavior (Supplementary Fig. S13). The dispersed and reversible polarization landscape also alleviates local electrostatic heterogeneity and electric-field concentration, promoting a more homogeneous local electric-field distribution and thereby contributing to the enhanced intrinsic breakdown strength.

This trend is further evidenced by the polarization magnitude and angle mappings shown in Fig. 4g, h. For 0BZN, distinct block-like polar regions are observed, which can be readily aligned under relatively low electric fields, accounting for its pronounced ferroelectric behavior. In contrast, 20BZN(H) exhibits highly heterogeneous distributions of both polarization magnitude and orientation, indicative of enhanced chemical disorder and local random fields arising from the high-entropy effect.

Statistical analysis of the local polarization distributions (Fig. 4i, j) reveals that the polarization displacement magnitude ranges from 0 to 25 pm, with average values (M_{ave}) of 8.58 and 6.82 pm for 0BZN and 20BZN(H), respectively. Despite the reduction in the average displacement magnitude, 20BZN(H) retains evident local polarization fluctuations, indicating that the synergistic effects of high-entropy engineering and compositional optimization effectively preserve localized polar distortions. Notably, both ceramics show nearly uniform polarization angle distributions with comparable fractions of R and T polar phases, reflecting a high degree of structural isotropy. In addition, monoclinic-like (M-like) transitional regions are identified, whose polarization vectors are oriented between those of the R and T phases[35], further evidencing the polymorphic nature of the local polarization configuration. Additional atomic-resolution HAADF-STEM analyses performed on multiple independent regions (Supplementary Fig. S14) reveal consistent polarization configurations, confirming that the observed local heterogeneous polarization structures are representative characteristics of the samples rather than isolated local features.

Taken together, these results confirm that 20BZN(H) inherits the intrinsic multiphase coexistence of the parent 0BZN ceramic, manifested as nanoscale polymorphic polarization configurations. More importantly, the high-entropy effect fragments the local polarization landscape into highly dispersed nanoscale regions while preserving strong local polarization fluctuations. Such nanoscale heterogeneity plays a critical role in achieving superior energy storage performance. On the one hand, the retained local polarization fluctuations enable the generation of large field-induced polarization under external electric fields. On the other hand, the fragmented polymorphic polarization configurations promote highly reversible polarization switching by reducing the domain-switching energy barrier and

https://doi.org/10.1038/s41467-026-79434-4

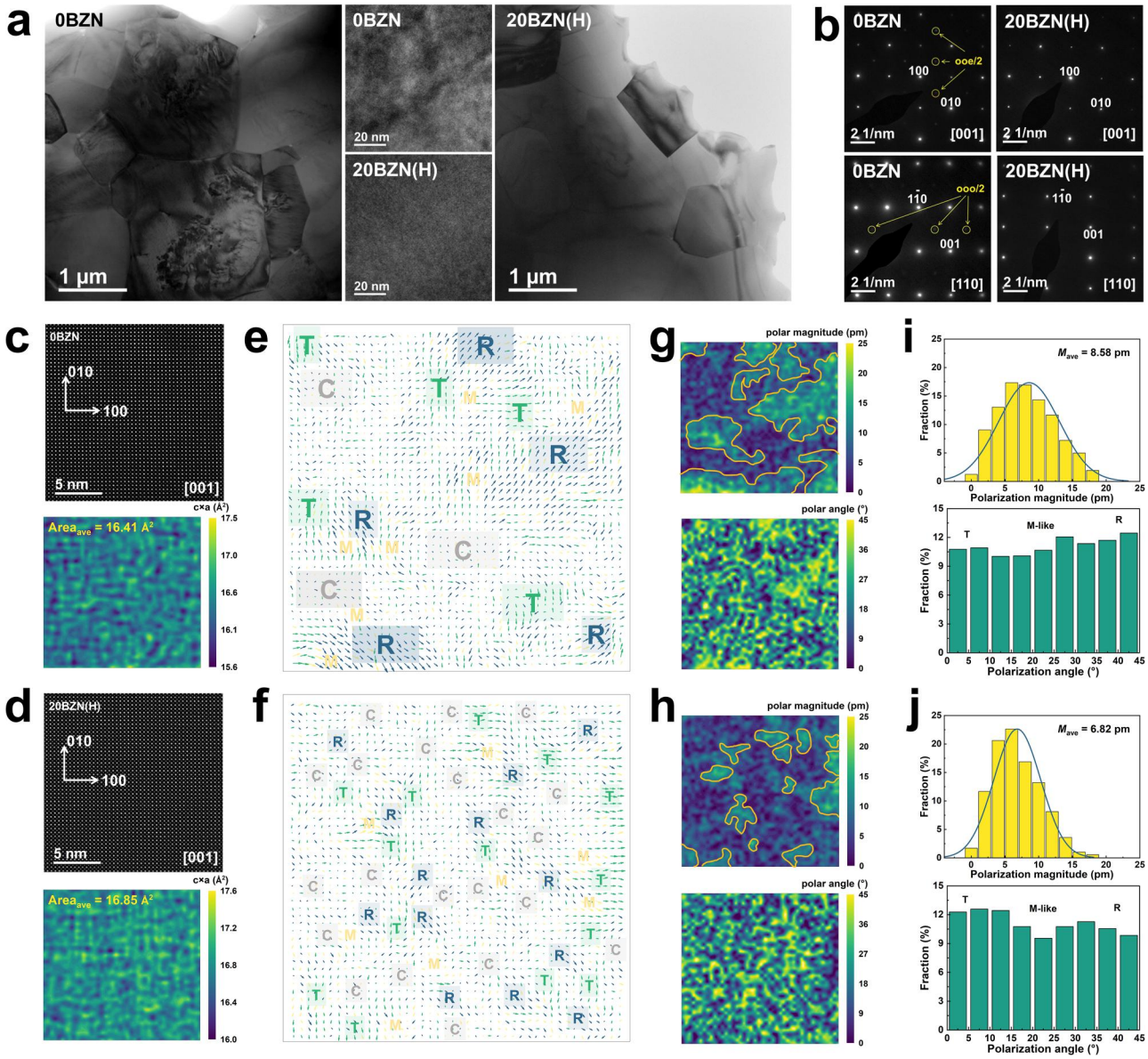


Fig. 4 | Domain structures and local polarization configurations of 0BZN and 20BZN(H) ceramics. a Low-magnification bright-field TEM and HRTEM images. **b** SAED patterns along the $[001]_c$ and $[110]_c$ zone axes. **c**, **d** Atomic-resolution HAADF-STEM images along the $[001]_c$ zone axis and the corresponding distributions of unit cell area. **e, f** Polarization vector mappings derived from the HAADF-STEM images in (**c**, **d**). **g**, **h** Spatial distributions and **i, j** statistical analyses of polarization angles and magnitudes. For clarity, the polarization angles were equivalently transformed into the range of 0–45° to distinguish different local symmetry states.

flattening the free-energy landscape, thereby minimizing hysteresis[36]. Meanwhile, the dispersed polarization landscape reduces local electrostatic heterogeneity and electric-field concentration, which is beneficial for dielectric breakdown strength. Consequently, the coexistence of strong local polar fluctuations and highly dynamic polymorphic polarization states provides an ideal balance between polarization development and reversibility, enabling the simultaneous realization of high P_{max}, ultralow P_r, and superior energy storage performance.

Local oxygen octahedral tilt

Dielectric energy storage performance is strongly influenced by BO_6 distortion, whose tilt magnitude and ordering degree play critical roles in governing polarization behavior under external electric fields. To elucidate the evolution of local BO_6 tilt configurations, atomic-resolution annular bright-field scanning transmission electron microscopy (ABF-STEM) images acquired along the $[001]_c$ zone axis were analyzed for 0BZN and 20BZN(H) ceramics (the tilt angle calculation method is provided in Supplementary Fig. S15). As shown in Fig. 5a, b, 0BZN exhibits pronounced BO_6 tilt, evidenced by the strong red-blue contrast, whereas 20BZN(H) displays evident weaker contrast, indicating a marked reduction in tilt amplitude accompanied by enhanced local structural disorder.

Fast Fourier transform (FFT) analysis (Fig. 5c, d) provides further evidence for this structural evolution. Distinct 1/2-type superlattice reflections are clearly observed in 0BZN but disappear in 20BZN(H), confirming the suppression of long-range ordered BO_6 tilt. Quantitative analysis of the local tilt distributions reveals two characteristic tilt configurations in 0BZN (Fig. 5e). Region I displays a long-range ordered structure characterized by periodically alternating clockwise and anti-clockwise tilts, with comparable average tilt angles of $A_{c\text{-}ave} = 2.50°$ and $A_{a\text{-}ave} = -2.55°$, respectively. Region II exhibits a

https://doi.org/10.1038/s41467-026-79434-4

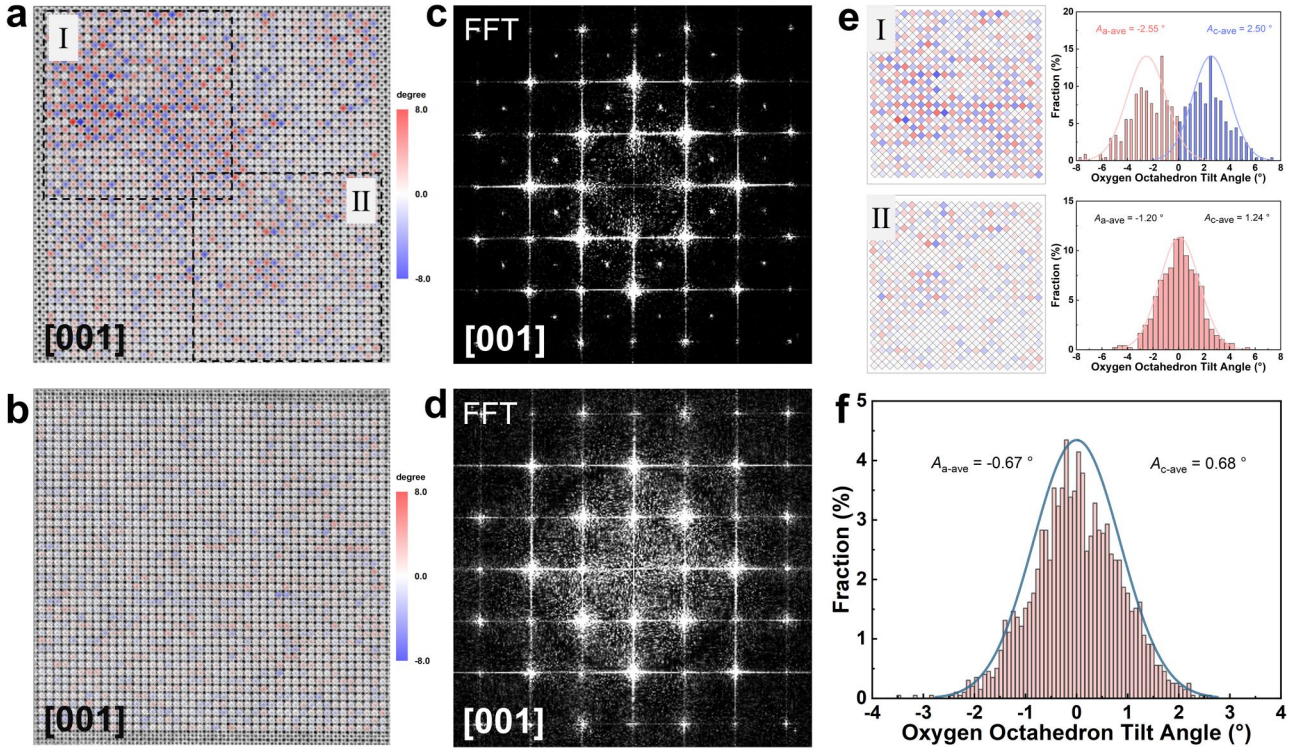


Fig. 5 | Local BO_6 tilt characteristics of 0BZN and 20BZN(H) ceramics. **a**, **b** Atomic-resolution ABF-STEM images acquired along the $[001]_c$ zone axis and the corresponding BO_6 tilt mappings for 0BZN and 20BZN(H). **c**, **d** FFT patterns derived from the ABF-STEM images shown in (**a**) and (**b**), respectively. **e**, **f** Statistical distributions of BO_6 tilt angles for 0BZN and 20BZN(H).

disordered tilt configuration characterized by randomly distributed tilts while retaining relatively large tilt amplitudes ($A_{c\text{-}ave} = 1.24°$, $A_{a\text{-}ave} = -1.20°$). The former is associated with long-range P4bm and R3c phases commonly observed in BNT-based ceramics, whereas the latter is associated with the short-range ordered structures within PNRs. In contrast, 20BZN(H) displays a highly disordered BO_6 tilt landscape, in which weak and sparse clockwise/anti-clockwise tilts are randomly embedded within a predominantly untilted matrix. Statistical analysis indicates that the tilt angles follow an approximately Gaussian distribution centered near zero, with average values of $A_{c\text{-}ave} = 0.68°$ and $A_{a\text{-}ave} = -0.67°$, both evidently smaller than those of 0BZN (Fig. 5f). Additional atomic-resolution ABF-STEM analyses performed on another independent region (Supplementary Fig. S16) reveal consistent BO_6 tilt configurations, confirming that the observed local BO_6 tilts are representative characteristics of the samples rather than isolated local features.

The evident suppression of BO_6 tilt in 20BZN(H) can be attributed primarily to the incorporation of large-radius Ba^{2+} ions, which expand the lattice and increase the tolerance factor. Consequently, the driving force for strain accommodation through oxygen octahedral rotation is reduced, leading to weakened BO_6 tilt and diminished lattice distortion. Combined with high-entropy engineering and high-energy ball milling, the local structure evolves from an ordered-tilt-dominated state to a weakly tilted and highly disordered configuration. Unlike the strong and ordered BO_6 tilt in 0BZN, which imposes structural constraints on polarization evolution, the weakened and disordered BO_6 tilt in 20BZN(H) reduces the coupling between local polarization and the long-range crystal framework and facilitates highly reversible field-induced polarization[20,23]. This leads to evidently reduced hysteresis loss and P_r, while alleviating structural constraints on polarization development. As a result, a high P_{max} is maintained alongside enhanced η, ultimately enabling superior energy storage performance.

Breakdown behavior and mechanisms

A high E_b is an indispensable prerequisite for realizing exceptional energy storage performance and is governed by both the intrinsic dielectric strength of the ceramic and extrinsic microstructural factors. As shown in Fig. 6a, the Weibull distributions of E_b of 100xBZN ceramics exhibit good linearity and high Weibull moduli ($\beta > 10$), confirming the reliability of the breakdown data. As shown in Fig. 6b and Supplementary Fig. S17, the average grain size (G_{ave}) gradually decreases with increasing S_{config}, accompanied by a corresponding increase in E_b. The inverse correlation between E_b and G_{ave} follows the empirical relationship $E_b \propto 1/G_{ave}$, indicating that the increased grain-boundary density resulting from grain refinement plays a critical role in enhancing breakdown strength[37]. The abundant grain boundaries act as effective barriers to charge transport and electrical-tree propagation, thereby suppressing breakdown failure. In addition, the enhanced relaxor characteristics induced by configurational-entropy engineering further contribute to the improvement of intrinsic breakdown strength. The formation of highly dispersed PNRs promotes a more homogeneous local electric-field distribution and alleviates field concentration, thereby reducing the probability of premature breakdown. The synergistic effects of grain refinement and entropy-induced relaxor behavior collectively account for the enhanced breakdown strength of the high-entropy ceramics. This interpretation is further supported by the complex impedance plots (Supplementary Fig. S18), which show a gradual increase in resistivity with increasing S_{config}, consistent with the enhanced relaxor behavior and the progressive improvement in breakdown strength.

Notably, as a result of the high-energy ball milling, 20BZN(H) exhibits a further reduction in average grain size (G_{ave} of ~0.8 μm) together with a lower pore density compared with 20BZN (Fig. 6c). The milled powders show finer and more uniformly distributed particles (Supplementary Fig. S19), indicative of an increased specific surface area and enhanced sintering reactivity. As a result, 20BZN(H)

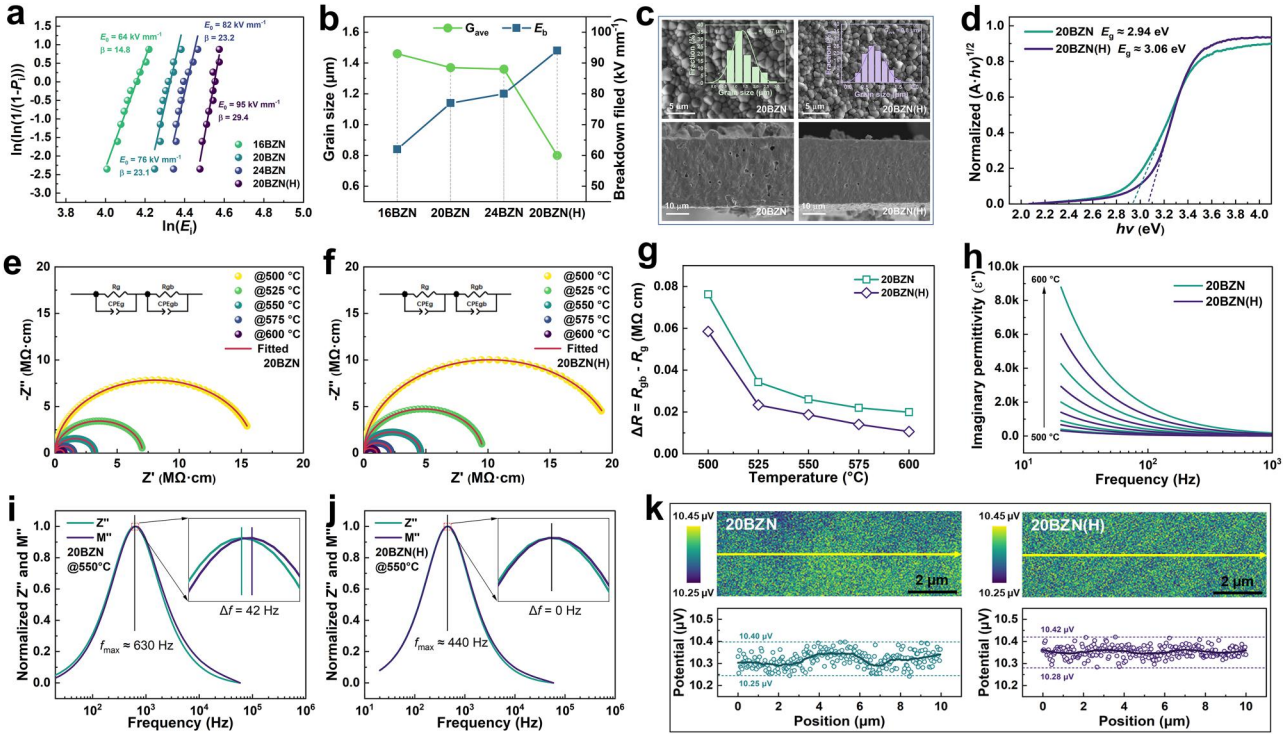


Fig. 6 | Breakdown behavior and underlying mechanisms. a Weibull distributions of E_b and **b** evolution of G_{ave} and E_b for high-entropy 100xBZN ceramics. **c** Microstructures, **d** E_g determined from the Tauc plots derived from the UV-Vis diffuse reflectance spectra, **e**, **f** complex impedance plots measured at 500–600 °C and the corresponding fitted curves for 20BZN and 20BZN(H), respectively, **g** deduced ΔR, and **h** frequency-dependent imaginary permittivity (ε'') of 20BZN and 20BZN(H). The Z''-f and M''-f spectra measured at 550 °C for **i** 20BZN and **j** 20BZN(H). **k** Surface potential maps and corresponding potential profiles of 20BZN and 20BZN(H).

develops a uniform and dense microstructure with refined grains, which provides a strong extrinsic contribution to the markedly enhanced E_b of 94 kV mm^{-1}. In addition to the microstructural optimization, 20BZN(H) exhibits an enlarged bandgap ($E_g \approx 3.06$ eV) compared with 20BZN ($E_g \approx 2.94$ eV) (Fig. 6d), suggesting enhanced intrinsic resistance to electronic conduction.

It is well recognized that interfacial polarization plays a critical role in determining E_b and is closely related to the size and distribution of grains and grain boundaries[7,25]. To further elucidate the role of electrical heterogeneity, temperature-dependent impedance spectroscopy was performed for 20BZN and 20BZN(H) at 500–600 °C. As shown in Fig. 6e, f, the complex impedance plots at all temperatures are well fitted by an equivalent-circuit model comprising grain and grain-boundary contributions, validating the extracted electrical parameters. Both the grain (R_g) and grain boundary (R_{gb}) resistances decrease with increasing temperature, consistent with thermally activated charge transport (Supplementary Fig. S20). Notably, the resistance contrast, defined as $\Delta R = R_{gb} - R_g$, is markedly reduced in 20BZN(H) throughout the entire temperature range (Fig. 6g). The reduced resistance contrast indicates a more homogeneous electrical environment between grains and grain boundaries, thereby suppressing interfacial charge accumulation and the associated interfacial polarization. Consistent with this interpretation, 20BZN(H) exhibits substantially lower imaginary permittivity (ε'') than 20BZN, particularly at low frequencies, and this suppression persists from 500 to 600 °C (Fig. 6h). The suppressed low-frequency ε'' further supports the reduced interfacial charge accumulation and associated dielectric loss in 20BZN(H). Figures 6i, j show the Z''-f and M''-f spectra of 20BZN and 20BZN(H) at 550 °C. The Z'' and M'' peaks correspond to distinct electrical relaxation processes associated with grain-boundary and grain responses, respectively, and their frequency separation (Δf) can be used to assess the degree of interfacial polarization[38–40]. In 20BZN, the Z'' and M'' relaxation peaks show a clear frequency separation of ~42 Hz, whereas they nearly overlap in 20BZN(H). The same trend is observed consistently across the entire temperature range (Supplementary Fig. S21). Together, the smaller ΔR, lower low-frequency ε'', and enhanced overlap of the Z'' and M'' peaks provide converging evidence that grain/grain-boundary electrical heterogeneity and the associated interfacial polarization are substantially suppressed in 20BZN(H). Consequently, the homogenized electrical environment suppresses interfacial charge accumulation and local electric-field concentration, thereby contributing to the enhanced breakdown strength.

To further verify the above conclusions, Kelvin probe force microscopy (KPFM) was employed to characterize the surface potential distributions (Fig. 6k). Compared with 20BZN, 20BZN(H) exhibits a more homogeneous surface-potential landscape with reduced local potential fluctuations, consistent with the suppressed interfacial polarization inferred from the impedance analysis. Quantitative fitting of the potential profile along the selected region (yellow line) further reveals a smaller potential variation and a smoother potential distribution in 20BZN(H), indicating enhanced electrical uniformity. In addition, 20BZN(H) exhibits a higher average surface potential, suggesting a higher energy barrier for carrier excitation from the Fermi level to the conduction band, which is beneficial for suppressing charge transport and enhancing the breakdown strength[41,42].

To further elucidate the contribution of microstructural optimization to breakdown strength, finite-element simulations of dielectric breakdown were performed for both 20BZN and 20BZN(H) using two-dimensional models reconstructed from SEM images (Supplementary Fig. S22). 20BZN(H) exhibits a markedly more homogeneous electric-field distribution, consistent with the suppression of interfacial polarization and local field concentration (Supplementary Fig. S23).

Moreover, the increased grain-boundary density results in a more tortuous breakdown path and effectively retards breakdown propagation. These characteristics collectively contribute to the enhanced breakdown resistance of 20BZN(H).

Taken together, these results demonstrate that configurational-entropy engineering enhances the intrinsic breakdown strength through the formation of highly dispersed PNRs, which improve local electric-field homogeneity, while high-energy ball milling provides additional extrinsic contributions through grain refinement, densification, and microstructural homogenization. The synergy between these intrinsic and extrinsic effects ultimately enables the enhanced breakdown strength achieved in 20BZN(H).

In summary, we demonstrate a dual-functional-unit modulation strategy to overcome the intrinsic polarization–breakdown trade-off in $Bi_{0.47}Na_{0.47}Ba_{0.06}TiO_3$-based relaxor ferroelectrics through the synergy of configurational-entropy engineering and microstructural optimization. Configurational entropy simultaneously tailors two key local functional units, leading to fragmented heterogeneous polarization states together with weakened and disordered BO_6 tilt, which together enable strong field-induced polarization, highly reversible polarization responses, and enhanced breakdown strength. In addition, grain refinement and densification induced by high-energy ball milling further suppress interfacial polarization and improve electrical homogeneity, contributing to the high E_b of 94 kV mm^{-1}, a large W_{rec} of 16.19 J cm^{-3}, and a high η of 91.3%. More importantly, this work identifies the cooperative regulation of local polarization and octahedral-tilt configurations as a general structural design principle for decoupling polarization response from dielectric breakdown, providing new insights for the development of high-performance dielectric energy storage materials.

Methods

Sample preparation

$(1\text{-}x)(Bi_{0.47}Na_{0.47}Ba_{0.06}TiO_3)\text{-}xBa(Zn_{1/3}Nb_{2/3})O_3$ ceramics (abbreviated as 100xBZN, x = 0, 0.12, 0.16, 0.20, 0.24) were synthesized using a conventional solid-state reaction method. High-purity Na_2CO_3 (99.8%), $BaCO_3$ (99.8%), Bi_2O_3 (99.99%), ZnO (99.9%), Nb_2O_5 (99.99%), and TiO_2 (98%) were used as starting materials for synthesizing $Bi_{0.5}Na_{0.5}TiO_3$ (BNT), $BaTiO_3$ (BT), and $Ba(Zn_{1/3}Nb_{2/3})O_3$ (BZN) powders. The precursor powders were then ball-milled for 4 h using alcohol as the milling medium. After drying, the BNT, BT, and BZN powders were calcined at 850 °C, 1050 °C, and 1020 °C for 4 h, respectively, followed by ball milling for an additional 24 h. Subsequently, the synthesized BNT, BT, and BZN powders were weighed and mixed according to the stoichiometric ratio of 100xBZN ceramics. The resulting mixture was blended with 6 wt.% polyvinyl butyral (PVB) as a binder and then pressed into pellets with a diameter of 10 mm and a thickness of 1 mm under a uniaxial pressure of ~400 MPa. The PVB was removed by heating at 550 °C for 2 h, and the pellets were then sintered at 1020–1150 °C for 2 h in sealed alumina crucibles to obtain the ceramic samples. To satisfy the requirements for energy storage characterization, 16BZN, 20BZN, and 24BZN high-entropy ceramics were fabricated as thick films using a tape-casting process. The as-prepared powders were mixed with a solvent (ethanol) and organic additives (PVB, dibutyl phthalate, and castor oil) in appropriate proportions, followed by ball milling for 0.5 h to obtain homogeneous casting slurries. The slurries were then cast onto PET carrier films using a tape caster and dried, after which green tapes with dimensions of 10 mm × 10 mm and a thickness of ~50 μm were cut. Prior to sintering, the samples were heated at 500 °C for 4 h to remove organic components. Subsequently, the samples were sintered at 1020–1060 °C for 3 h, yielding dense ceramic thick films with final thicknesses of approximately 30–35 μm.

Structure characterization

The X-ray diffraction (XRD) patterns were recorded using an X-ray diffractometer (D8 Advance, Bruker, Germany) with Cu Kα radiation (λ = 1.54 Å). The Raman spectra were obtained using a Raman spectrometer (Horiba Jobin Yvon HR800, France) with a 532 nm excitation laser. The microstructure was examined using scanning electron microscopy (Hitachi SU-5000 FE-SEM, Japan). Domain morphologies, selected-area electron diffraction (SAED) patterns, and high-resolution images were obtained using a transmission electron microscope (TEM, Talos F200X, FEI, USA). High-angle annular dark-field (HAADF) images and energy-dispersive spectroscopy (EDS) mapping were conducted using an atomic-resolution scanning transmission electron microscope (STEM, Thermo Scientific Spectra 300). Polar vector calculations were performed using Python scripts and MATLAB algorithms based on the brightness contrast in high-resolution atomic images. UV-Vis diffuse reflectance spectra were recorded using a spectrophotometer (Cary 5000 UV-Vis-NIR, Agilent Technologies, USA).

Electrical characterization

For energy storage performance characterization (unipolar P–E loops), gold electrodes with an area of 1 mm^2 were deposited by sputtering. The unipolar P–E hysteresis loops were recorded at 10 Hz using a ferroelectric analyzer (aix-ACCTF Analyzer 2000, Aachen, Germany). The dielectric properties and complex impedance spectra were measured using an impedance analyzer (E4990A, Keysight, USA). The charge-discharge performances were characterized using a charge-discharge apparatus (PK-CPR1801-10015, Polyk Technology, State College, USA) with a specific discharge resistance (10 kΩ) in an RLC circuit. Piezoresponse Force Microscopy (PFM) measurements were carried out to characterize the surface morphology, phase, and amplitude responses under external electric fields (MFP-3D, Asylum Research, USA). The surface potential was measured using Kelvin probe force microscopy (KPFM, Bruker Icon).

Data availability

The source data underlying all graphs and charts presented in the main figures and Supplementary Figs. are available in the Source Data file deposited in Figshare at https://doi.org/10.6084/m9.figshare.34030947. All other data supporting the findings of this study are available within the article and its Supplementary Information files. Any data deemed relevant are available from the corresponding author upon request (daiyj8@mail.sysu.edu.cn).

References

1. Yang, L. T. et al. Perovskite lead-free dielectrics for energy storage applications. *Prog. Mater. Sci.* **102**, 72–108 (2019).
2. Zubairi, H. et al. Current development, optimisation strategies and future perspectives for lead-free dielectric ceramics in high field and high energy density capacitors. *Chem. Soc. Rev.* **53**, 10761–10790 (2024).
3. Zhu, W. et al. A review: (Bi,Na)TiO_3 (BNT)-based energy storage ceramics. *J. Mater.* **10**, 86–123 (2024).
4. Yan, F. et al. Progress and outlook on lead-free ceramics for energy storage applications. *Nano Energy* **123**, 109394 (2024).
5. Yang, Z. T. et al. High-performance lead-free bulk ceramics for electrical energy storage applications: design strategies and challenges. *J. Mater. Chem. A* **9**, 18026–18085 (2021).
6. Wang, G. et al. Electroceramics for high-energy density capacitors: current status and future perspectives. *Chem. Rev.* **121**, 6124–6172 (2021).
7. Cao, W. J. et al. Breaking polarization-breakdown strength paradox for ultrahigh energy storage density in NBT-based ceramics. *Nat. Commun.* **16**, 6228 (2025).
8. Jayakrishnan, A. R. et al. Are lead-free relaxor ferroelectric materials the most promising candidates for energy storage capacitors?. *Prog. Mater. Sci.* **132**, 101046 (2023).

9. Wang, Z. et al. Ultra-high energy storage in lead-free $NaNbO_3$-based relaxor ceramics with directional slush-like polar structures design. *Nat. Commun.* **16**, 2892 (2025).
10. Wei, T. et al. High-entropy assisted capacitive energy storage in relaxor ferroelectrics by chemical short-range order. *Nat. Commun.* **16**, 807 (2025).
11. Huang, Y. et al. Ultrahigh energy storage capacities in high-entropy relaxor ferroelectrics. *J. Mater. Chem. A* **12**, 18224–18233 (2024).
12. Xie, A. W. et al. Superior capacitive energy storage of $BaTiO_3$-based polymorphic relaxor ferroelectrics engineered by mesoscopically chemical homogeneity. *Adv. Sci.* **12**, 2502916 (2025).
13. Jiao, Y. et al. Overview of high-entropy oxide ceramics. *Mater. Today* **77**, 92–117 (2024).
14. Zheng, B. et al. High entropy-driven large capacitive energy storage in BaTiO3-based multilayer ceramic capacitors. *Adv. Energy Mater.* **16**, e04126 (2025).
15. Kong, X. et al. High-entropy engineered $BaTiO_3$-based ceramic capacitors with greatly enhanced high-temperature energy storage performance. *Nat. Commun.* **16**, 885 (2025).
16. Chen, L. et al. Giant energy-storage density with ultrahigh efficiency in lead-free relaxors via high-entropy design. *Nat. Commun.* **13**, 3089 (2022).
17. Zhou, X. F. et al. High-entropy ferroelectric-ferroelastic hybrid for ultrahigh and temperature-insensitive dielectric energy storage. *Adv. Sci.* **13**, e18725 (2025).
18. Duan, J. et al. High-entropy superparaelectrics with locally diverse ferroic distortion for high-capacitive energy storage. *Nat. Commun.* **15**, 6754 (2024).
19. Xie, A. W. et al. Superior capacitive energy storage of $NaNbO_3$-based MLCCs enabled by heterogeneous short-range ferroic orders. *Adv. Funct. Mater.* **36**, e16297 (2025).
20. Qi, H. et al. Large (anti)ferrodistortive $NaNbO_3$-based lead-free relaxors: polar nanoregions embedded in ordered oxygen octahedral tilt matrix. *Mater. Today* **60**, 91–97 (2022).
21. Wei, K. et al. Collaborative design of polarization and antiferrodistortion configurations in high energy capacitive relaxor ferroelectrics. *Nat. Commun.* **16**, 7833 (2025).
22. Chen, L. et al. Design of hierarchical-heterostructure antiferroelectrics for ultrahigh capacitive energy storage. *Nat. Commun.* **16**, 10668 (2025).
23. Chen, L. et al. Ultrahigh capacitive energy storage in lead-free relaxors via localizing distortion. *ACS Nano* **19**, 17738–17745 (2025).
24. Zhang, M. et al. Microstructure control on optimizing energy storage performance for dielectric ceramic. *Rev. Mater. Res.* **1**, 100006 (2025).
25. Cao, W. et al. Interfacial polarization restriction for ultrahigh energy-storage density in lead-free ceramics. *Adv. Funct. Mater.* **33**, 2301027 (2023).
26. Cao, W. et al. Interfacial-polarization engineering in bnt-based bulk ceramics for ultrahigh energy-storage density. *Adv. Sci.* **11**, 2409113 (2024).
27. Chen, L. et al. Outstanding energy storage performance in high-hardness $(Bi_{0.5}K_{0.5})TiO_3$-based lead-free relaxors via multi-scale synergistic design. *Adv. Funct. Mater.* **32**, 2110478 (2022).
28. Wang, X. et al. Optimizing the grain size and grain boundary morphology of $(K,Na)NbO_3$-based ceramics: paving the way for ultrahigh energy storage capacitors. *J. Mater.* **7**, 780–789 (2021).
29. Coondoo, I. et al. A comparative study of structural and electrical properties in lead-free BCZT ceramics: Influence of the synthesis method. *Acta Mater.* **155**, 331–342 (2018).
30. Balachandran, P. V. et al. Predicting displacements of octahedral cations in ferroelectric perovskites using machine learning. *Acta Crystallogr. B* **73**, 962–967 (2017).
31. Sun, Z. et al. Strong local polarization fluctuations enabled high electrostatic energy storage in Pb-free relaxors. *J. Am. Chem. Soc.* **146**, 13467–13476 (2024).
32. Chen, L. et al. Near-zero energy consumption capacitors by controlling inhomogeneous polarization configuration. *Adv. Mater.* **36**, 2313285 (2024).
33. Glazer, A. M. The classification of tilted octahedra in perovskites. *Acta Crystallogr. B* **28**, 3384–3392 (1972).
34. Pan, H. et al. Ultrahigh-energy density lead-free dielectric films via polymorphic nanodomain design. *Science* **365**, 578–582 (2019).
35. Guo, J. et al. Multi-symmetry high-entropy relaxor ferroelectric with giant capacitive energy storage. *Nano Energy* **112**, 108458 (2023).
36. Liu, Y. et al. Harnessing local inhomogeneity for enhanced dielectric energy storage. *Nat. Commun.* **16**, 6236 (2025).
37. Tunkasiri, T. et al. Dielectric strength of fine grained barium titanate ceramics. *J. Mater. Sci. Lett.* **15**, 1767–1769 (1996).
38. Zhao, H. et al. High-entropy design toward ultrahigh energy storage density under moderate electric field in bulk lead-free ceramics. *Adv. Funct. Mater.* **35**, 2411954 (2024).
39. Wang, C. et al. Equimolar high-entropy for excellent energy storage performance in $Bi_{0.5}Na_{0.5}TiO_3$-based ceramics. *Energy Storage Mater.* **70**, 103534 (2024).
40. Wang, C. et al. Ultrahigh energy-storage density of $BaTiO_3$-based ceramics via the interfacial polarization strategy. *ACS Appl. Mater. Interfaces* **15**, 42774–42783 (2023).
41. Ma, R. et al. Boosting the energy storage performances of Dy_2O_3-modified $Pb_{0.95}La_{0.02}Ca_{0.03}(Zr_{0.6}Sn_{0.4})_{0.995}O_3$ antiferroelectric ceramics via the grain boundary effect. *ACS Appl. Mater. Interfaces* **18**, 10057–10066 (2026).
42. Wu, J. et al. Nano-micro engineering modulating high-entropy multilayer ceramic capacitor for high-performance energy storage. *Adv. Funct. Mater.* **36**, e14008 (2025).

Author contributions

This work was conceived and designed by Y.J.D., H.Q., and B.L.; G.F.L. fabricated the samples, tested the energy-storage, stability, structure, and other properties, and processed related data, assisted by J.Y.W.; The finite element simulation was processed by B.O., X.Q.C., and Y.C.; The dielectric spectra, optical absorption spectra and impedance spectra were collected by X.Y.C. and R.G.; The SEM, TEM and HAADF-STEM images were collected and processed by G.F.L.; The manuscript was drafted by G.F.L., and revised by Y.J.D., H.Q., and B.L.; All authors participated in the data analysis and discussions.

Funding

This work was supported by the National Natural Science Foundation of China (52172135), the Youth Top Talent Project of the National Special Support Program (2021-527-07), the Leading Talent Project of the National Special Support Program (2022WRLJ003), and Shenzhen Science and Technology Program (Grant No. JCYJ20240813151421028).

Competing interests

The authors declare no competing interests.

Additional information

Supplementary information The online version contains supplementary material available at https://doi.org/10.1038/s41467-026-79434-4.

Correspondence and requests for materials should be addressed to Bin Li, He Qi or Yejing Dai.

Peer review information *Nature Communications* thanks Ganghua Zhang, and the other, anonymous, reviewer(s) for their contribution to the peer review of this work. A peer review file is available.

Reprints and permissions information is available at http://www.nature.com/reprints

Publisher's note Springer Nature remains neutral with regard to jurisdictional claims in published maps and institutional affiliations.

Open Access This article is licensed under a Creative Commons Attribution-NonCommercial-NoDerivatives 4.0 International License, which permits any non-commercial use, sharing, distribution and reproduction in any medium or format, as long as you give appropriate credit to the original author(s) and the source, provide a link to the Creative Commons licence, and indicate if you modified the licensed material. You do not have permission under this licence to share adapted material derived from this article or parts of it. The images or other third party material in this article are included in the article's Creative Commons licence, unless indicated otherwise in a credit line to the material. If material is not included in the article's Creative Commons licence and your intended use is not permitted by statutory regulation or exceeds the permitted use, you will need to obtain permission directly from the copyright holder. To view a copy of this licence, visit http://creativecommons.org/licenses/by-nc-nd/4.0/.

© The Author(s) 2026

This Article in Press is shared early to give you faster access to new research. It is citable and carries a permanent DOI. The final edited version will replace it automatically.